Chapter 4

Use of Guided Wave Thickness Resonance for Monitoring Pipeline Wall Thinning Using an Internal PIG

Ángela Angulo, Slim Soua and Tat-Hean Gan

Additional information is available at the end of the chapter

http://dx.doi.org/10.5772/62985

Abstract

Experimental data and modelling results for pipeline wall thinning confirm a classification of Guided Wave (GW) propagation and detected features based on signal amplitude. This interpretation leads to a decision on a follow up inspection based on High, Medium or Low priority. The severity of defects must be determined; achievable by examining the signal amplitude as a function of metal loss. Specifically, if resonance can be obtained at a particular frequency, the operator can identify the wall thickness loss through the reflected GW energy amplitude. Previous research presented in this chapter identified a suitable strategy to deploy this thickness resonance technique, starting from dispersion curves (DC) development, to the analysis of the thickness loss effect on the DC, and experiments that prove the effectiveness of the methodology.

Keywords: long-range ultrasonic, pipe thinning monitoring, corrosion, high-frequency-guided waves, thickness resonance technique

1. Introduction

Around 0.5 million kilometres of buried oil pipelines in Europe carry hazardous fluids [1] often at high pressure and temperature. In Europe alone, up to four million gallons of oil per year are leaked into the environment due to corrosion and mechanical damage. Pipeline spills of hazardous fluids into the environment outnumber all other sources (e.g. tanker spills in oceans, etc.) combined. The pipeline network in Europe is increasing at a rate of about 1000 km per year [2]. With this rapid expansion and the existing ageing pipeline (>30 years old), there is a growing growing challenge to maintain its structural integrity. Finding and repairing

pipe damage before catastrophic failure occurs, particularly as buildings encroach on pipeline sites, is crucial. Existing inspection using 'intelligent pigs' to find potentially harmful damage and repair or replacement by digging trenches to expose the pipe is very difficult at river, rail and road crossings. Yet, a typical 100-km pipeline might cross six rivers, four railways and three motorways as well as numerous other road crossings [3]. Between 1990 and 2000, there were an average of 75 pipe leakage incidents releasing oil onto land, into rivers and into underground water[4]. To address this issue, pressure is being put on pipeline operators to find new inspection technologies, which provide early warning of pipes at risk of failure [5]. In Brussels, European Union officials have urged 15 government members to begin applying new inspection, re-welding, and repair rules and technology to stem this pollution [6].

Oil and gas transmission lines are generally owned by specialist distribution companies. They usually have only a small technical and engineering base so most of their maintenance activities are outsourced. This is particularly true in the areas of inspection, non-destructive testing (NDT), machining and welding [7]. Estimates put these markets as growing annually by 10% [8]. If current methods of ultrasonic NDT were deployed, aiming to achieve full volume coverage, the position of conventional ultrasonic probes, for example, compression or electromagnetic acoustic transducer (EMAT) probes, would have to be adjusted every few millimetres to keep them in contact or in close proximity with the walls through long lengths of pipeline making it extremely difficult to achieve in practice with a small robot.

Most pipelines are buried in the ground and, once buried, every effort is made to leave them there. Excavation is not only expensive but the site conditions under which any repairs, re-welding or replacements are made are so poor that new defects can be introduced. Excavation is even more problematic when the pipeline is buried under rivers, railways and roads, where damage is more prevalent. Inspection and any repairs need to be conducted with the minimum of disruption, avoided by internal inspections using inspection robots (pigs) although repairs necessarily require the pipeline to be excavated.

The pigs occupy the entire cross section of a pipe due to the size of the sensor collar assembly needed to provide 100% volume coverage. Pigs can cope with moderate changes in diameter and moderate bends in the pipeline but there is a large variation in pipe sizes, for example, standard welded steel pipelines for gas/crude/oil product have internal diameters between 150 and 350 mm while larger pipes have an internal diameter from 500 to 1380 mm. Therefore, a matching pig is required for each pipe size, and for larger diameters the pigs tend to be very bulky. About one-third of all pipelines worldwide are considered unpiggable by existing smart pigs because of difficult access (launching and receiving facilities), restrictions due to valves, substantial changes in diameter along the length of the pipeline, small radius bends, dented or collapsed areas, excessive debris or scale build-up, impassable fittings, low operating pressure, low flow or absence of flow and other configuration issues [9].

The most common type of pig uses Magnetic Flux Leakage (MFL) techniques. These techniques are sensitive to changes in the flux of a strong magnetic field induced in the pipe wall as the 'pig' passes through. Sensors detect leakage of the flux from the pipe wall due to changes in the volume of the wall caused by corrosion, cracks, welds, bends and other geometric effects. MFL pigs however cannot distinguish acceptable anomalies from defects, or determine

http://dx.doi.org/10.5772/62985

whether the indication is from the external or internal surface. It also cannot determine the circumferential location of the signal. This technique is also limited to pipes not encased by steel conduits, which is often the case for road and rail crossings.

Using Long Range Ultrasonic Testing (LRUT), sensors need to be adjusted only every 50-150 m, the typical attainable propagation range of GW waves in pipelines, , thus facilitating mechanical adaptation. Data volumes are greatly reduced compared to conventional ultrasound. LRUT can also be deployed internally for pipeline inspection [10]. The advantage of LRUT is a data volume orders of magnitude lower than conventional ultrasound to provide 100% pipe volume coverage [11]. Results can potentially be processed faster with less labour required subsequent to the pigging operation. This advantage is achieved at the expense of loss in sensitivity, with minimum detectable defect sizes much larger than are achievable with conventional ultrasound. with conventional ultrasound. However, LRUT allows serious defects needing immediate attention to be detected far more rapidly.

The identification of defects remains difficult and misinterpretation of indications can have disastrous consequences. For example [12], misinterpretation of a dent in a 16" gasoline line as an innocuous weld manufacturing flaw led to the release of 237,000 gallons of fuel into Whatcom Falls Park, Washington State, USA, which subsequently ignited killing three young boys and landed BP-Amoco with a $3million penalty [13]. To guarantee proper evaluation of all indications detected with the 'intelligent pig', the pipe must be 'dug out', exposed and tested from the outside with more sensitive NDT techniques such as ultrasonics. This is applied manually and are not sufficiently accurate for Fitness for Service (FFS) assessment. Any potentially damaged section of the pipe is therefore replaced with a new section or 'pup-piece', which is welded into the pipeline at either end with butt welds. Certainly, the excavated pipeline must be inspected again before being re-buried.

2. Background

The LRUT or MFL approaches determine and extract damage-sensitive features from the signal using different signal-processing algorithms. A pattern recognition technique is then required to classify the damage and estimate its severity. It is important to note that Structural Health Monitoring (SHM) always involves the use of threshold values to decide on damage presence in the structure. The choice of the threshold is usually application-dependent and typically relies on some false-positive probability estimation [14]. It is assumed that a signal-to-noise ratio of 6 dB is required for detection in order to reduce the number of false indications. With this in mind, the required sensor detection performance can be evaluated [13]. However, it is not an objective assessment as the nature of the defects themselves requires more detailed interpretation. understanding. For this reason, the requirement of the implementation of GW SHM must involve the detailed characterisation and understanding of the response from the various types and sizes of defects[15]. In [16], the authors assess the feasibility of a monitoring process on an aluminium plate and steel pipe, and damage was simulated by changing the boundary conditions of each structure [14]. It is also crucial to identify a formal classification

routine that characterise flaw severity using GW. Damage can be incrementally introduced into the structure, and at each depth multimode wave signals can relate the changes in received signal due to mode conversion and scattering from the flaw.

Lamb wave tomography reconstructions can be used by incorporating several different analysis techniques including wavelet-based feature extraction, and formal pattern classification to create a fully-automated analysis scheme designed to locate, size and identify the severity of unknown flaws. Variations of Lamb wave propagation reflect changes in effective thickness and material properties caused by structural flaws as corrosion, fatigue cracks and voids that can then be mapped via a reconstructed tomographic image [17]. In [18], an extension of classical imaging techniques that take advantage of the chirplet-based matching pursuit algorithm was presented. For non-dispersive propagation, an accurate localisation can be obtained. Even if specific low-dispersive modes are injected, mode conversion at discontinuities can generate dispersive modes superimposed on the targeted modes. This effect significantly complicates the measurements and demonstrates the need for pattern recognition algorithms which can be trained through either modelled or experimental data. The fundamental concept of class distribution within each feature space was discussed in [19] and features were correctly identified with respect to their severity. A linear spread of classes would allow new data corresponding to an intermediate flaw depth to fall correctly between classes, in order to identify a feature space where the classes are mostly linearly distributed.

The approach using torsional ultrasonic GW has strong potential for prognostics-based structural health management due to strong correlation and relationship between damage size change and the signal deviation demonstrated using the error function (erf). This process is effective in monitoring crack growth and shows an evaluation of the Probability of Detection (PoD). The Euclidian distance, which is defined essentially as the signal-to-baseline ratio, was used.

3. Numerical modelling analysis

In this section, the theoretical background to the numerical modelling of GW is presented. Elastodynamic equations govern the dynamic behaviour of a homogeneous linear elastic material. The weak formulation is detailed and provides the equations solved numerically to describe the wave propagation in the pipes. The cross section of the pipe is divided in the thickness direction into layered elements, and waves in the propagating direction z are described by the orthogonal function $e^{(i\xi z)}$, where ξ is the wave number. The mth eigenvalue ξm of the Eigen system derived here denotes the wave number of the mth mode. The elastodynamic variational formulation will be described leading to the discretization of the Finite Element formulation [20]:

$$\int_{\Omega} \delta\varepsilon_{ij}.C_{ik}.\varepsilon_{kj}\partial\Omega + \rho\omega^2 \int_{\Omega} \delta U_i.U_i\partial\Omega + \int_{\Sigma} \delta U_i.\left[\sigma_{ij}.n_j\right]\partial\Sigma = 0$$

http://dx.doi.org/10.5772/62985

The proposed formulation allows the description of wave propagation in complex geometries including oval cross sections induced by external pressure acting on offshore pipes. This aspect will be thoroughly described in this section.

The modelling work presented next predicts the propagation of the GW modes in an isotropic structure containing discontinuities. The key point is to decompose the returning signal into the mode content with regard to the wave-number scale and the frequency. This is obtained through the use of two-dimensional (2D) Fourier transform applied to A-scans obtained for discretised locations along the structure's length.

In the stationary regime domain model, it is possible to plot the frequency spectrum of the GW and compare it to the spectrum of a structure containing a discontinuity. The discontinuity considered here was a thinned region of about 20cm length, representing a corroded or metal loss area.

The second part of the modelling work is based on transient lamb wave excitation in the structure with a discontinuity. The choice of the frequency range of operation uses conclusions obtained in part 1 of the work. The aim of this part is to prove how realistic the stationary calculation results are. A Fast Fourier transform is used to extract the mode contents from the A-scans.

The final part of this work is based on the 2D fast Fourier transform, proven to be an efficient tool of mode identification. The content of the obtained A-scans is clearly affected by the discontinuity and more modes are generated dependent on the discontinuity thickness (and therefore the remaining thickness). Finally, structures with different notches depths were tested.

3.1. The stationary regime

It is possible to separately excite the symmetric and the asymmetric waves in a plate; this is achieved based on the following choices:

- To excite an S0 mode, tangential symmetric and normal asymmetric displacements should be excited.
- To excite an A0 mode, normal and tangent displacement excitation should be inverted.

The statement of the modelling problem uses the following assumptions:

- The solution is obtained in the harmonic domain; this supposes the excited wave to have a single frequency.
- The solution is obtained based on the stationary solver using Finite Element Analysis (FEA).
- The meshing is 2500 elements along a 1 m length.

Figure 1 shows the separation of the resulting symmetrical and asymmetrical displacements. It is proved that the resulting S0 displacement mode is normal; however, the resulting A0 displacement mode is tangent. At this stage, the FEA model seems consistent with the initial assumptions.

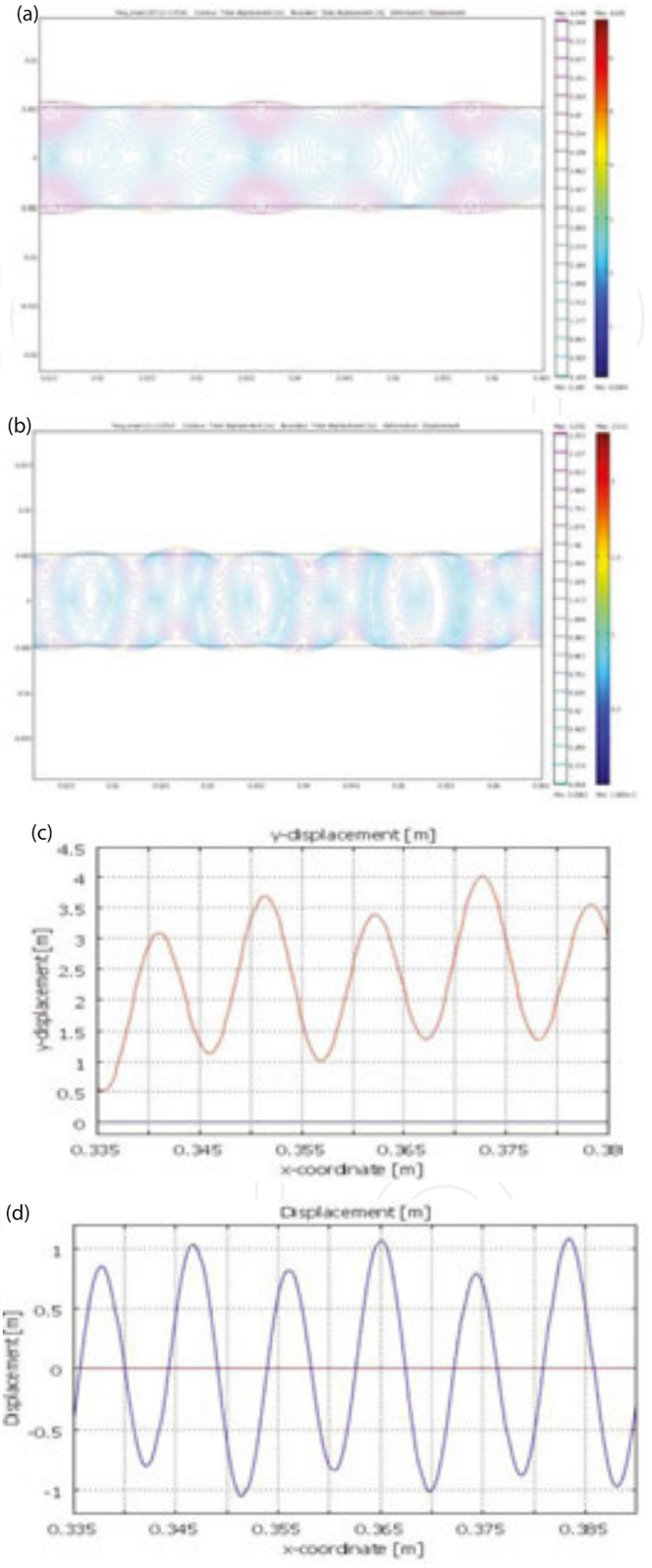

Figure 1. Displacement plots obtained for selective excitation of S0 and A0 modes, respectively. (a) Displacement for S0 mode at 307kHz. (b) Displacement for A0 mode at 307kHz. (c) Displacements along neutral plane for S0 excitation. Lambda=9.7mm. (d) Displacements along neutral plane for A0 excitation. Lambda=8.7mm.

http://dx.doi.org/10.5772/62985

In the next step, a frequency sweep is performed in order to generate a spectrum of the resulting A-scan. The previous excitation models were used and the frequency spectra of the S0 and A0 modes were plotted for a homogeneous plate (constant thickness).

Figure 2 shows the superposition of the frequency spectra for the frequency range [200 - 400kHz] and the displacement resonances. In this specific frequency range, we expect to obtain the natural resonance. The displacement plot shows that the obtained results are in agreement with the previous assumption and the expected modes are obtained.

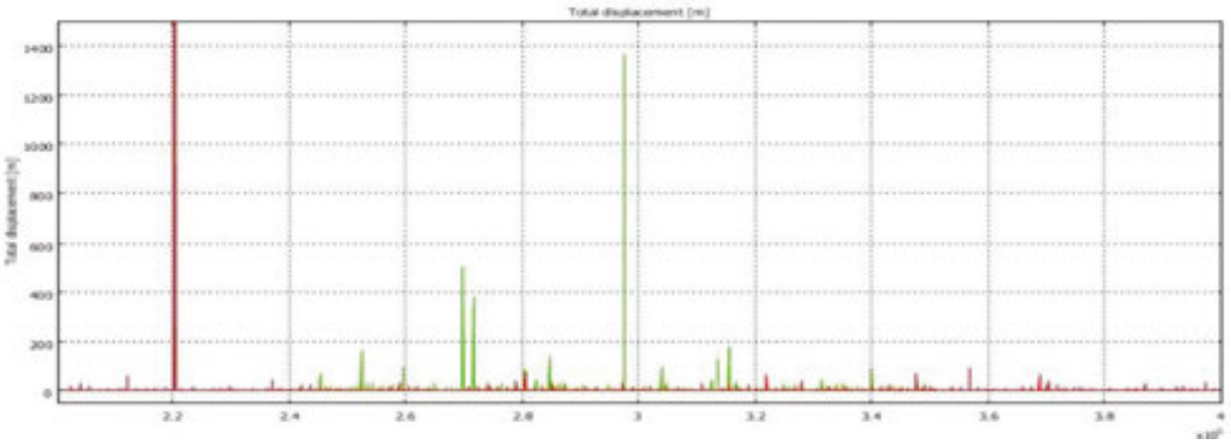

Figure 2. Superposition of spectra obtained for S0 (green) excitation and A0 (red) excitation in a plate.

The next step is to build a spectrum of the plate with a 5mm thickness discontinuity (**Figure 3**) and compare it to the previous spectrum of the defect-free plate (**Figure 4**).

Figure 3. Thickness reduction in a plate of 10 mm.

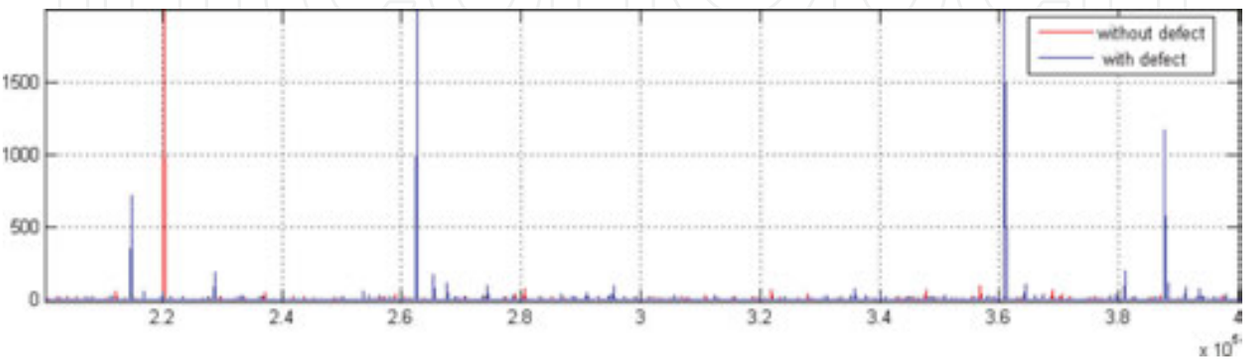

Figure 4. Superposition of spectrum obtained for uniform plate and 'defective' plate.

3.2. Displacement visualisation of resonant frequency for plate with thickness change

Localised thickness reduction was introduced along 10 cm length, 40 cm from the excited edge (**Figure 3**). In the frequency spectrum of the defective plate, compared to the spectrum of the defect-free plate, resonances occurred at 214.8, 262.2, 360.9 and 387.7 kHz. The displacement plots of the excited GW at these frequencies are presented in **Figures 5–8**, the normal and tangential displacement components of an excited pure Lamb (A or S) mode are plotted at the neutral plane of the main plate (e = 10 mm). One of the displacement components is supposed to vanish; the other component is then obtained in the form of the propagating Lamb mode with a constant wave number.

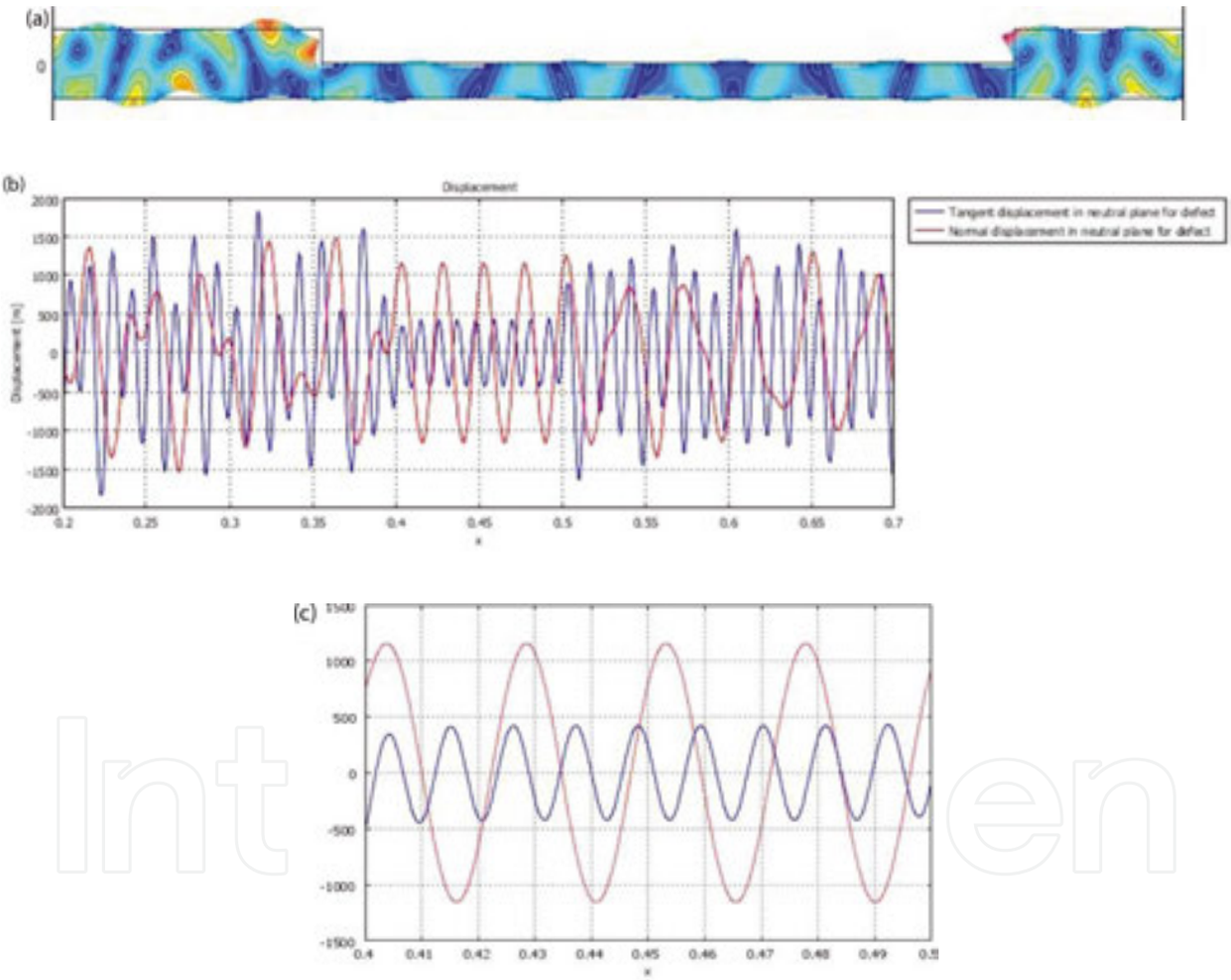

Figure 5. Displacement plots of the excited guided waves at 214.8 kHz. (a) Wave propagation-amplitude plot. (b) Displacement components at y=5 mm. (c) Zoom on the thinner zone.

http://dx.doi.org/10.5772/62985

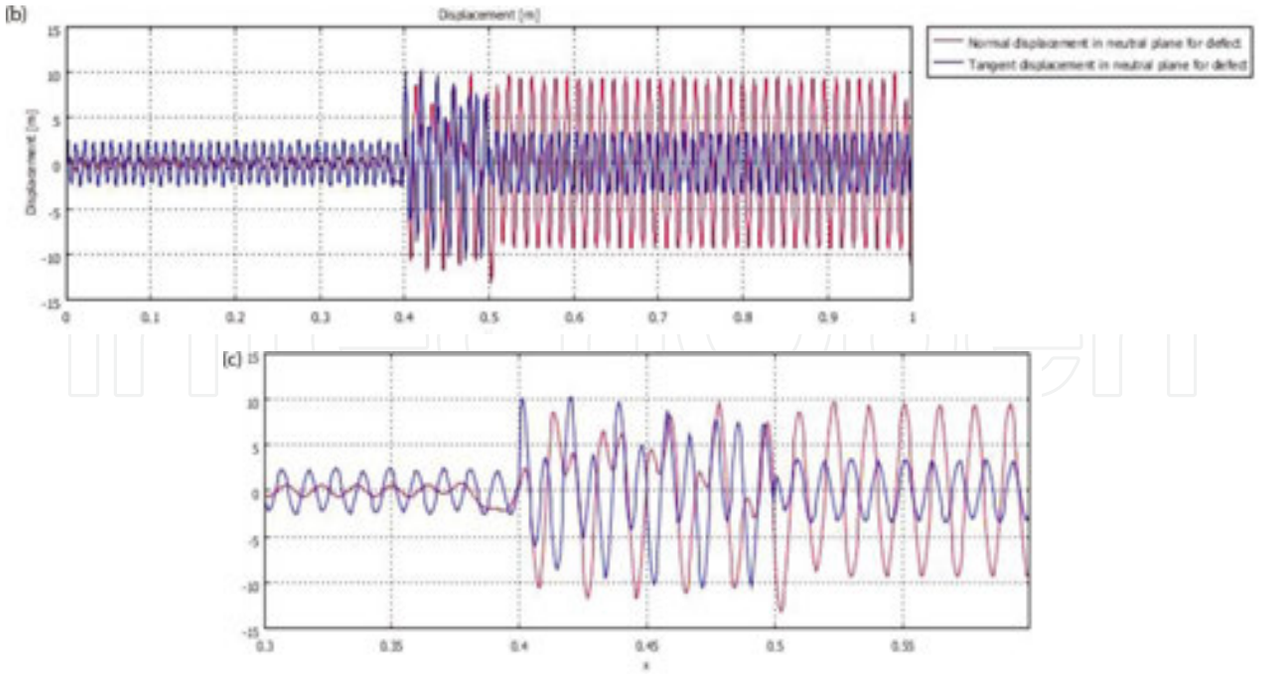

Figure 6. Displacement plots of the excited guided waves at 262.2 kHz. (a) Wave propagation-amplitude plot. (b) Displacement components at y=5 mm. (c) Zoom on the 5mm thickness zone.

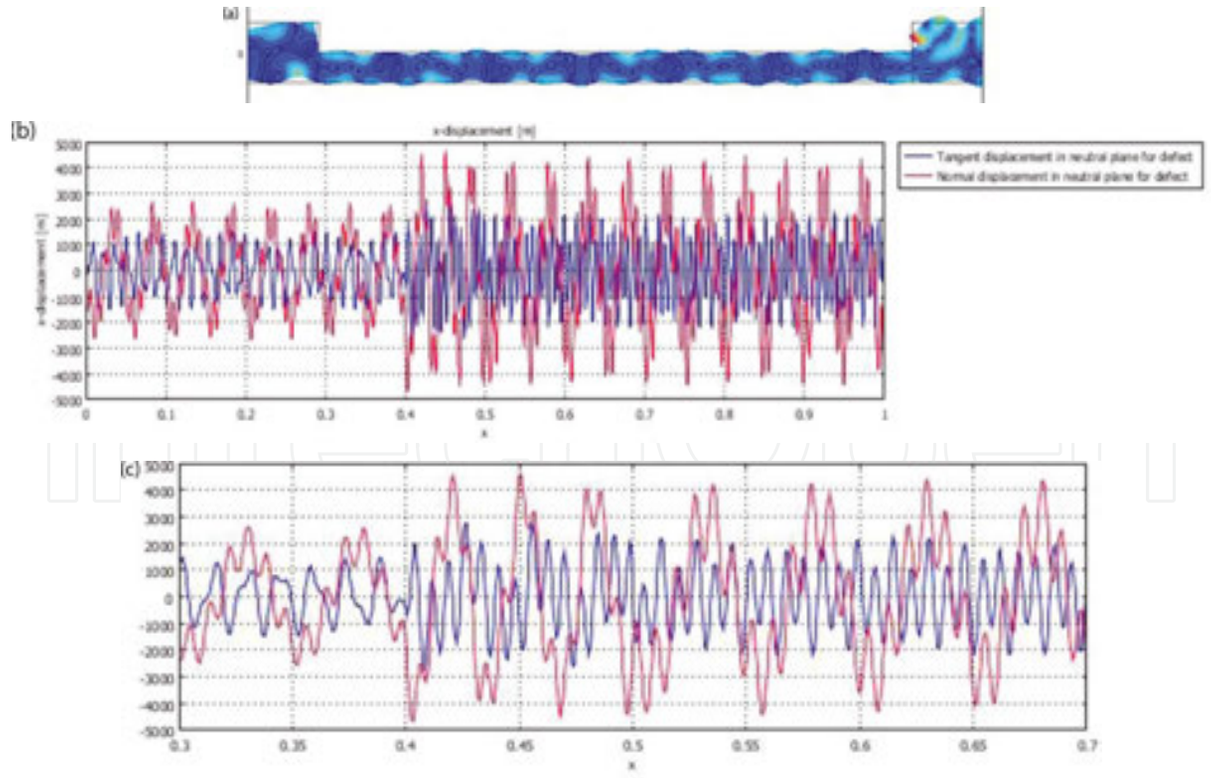

Figure 7. Displacement plots of the excited guided waves at 360.9 kHz. (a) Wave propagation-amplitude plot. (b) Displacement components at y=5 mm. (c) Zoom on the 5 mm thickness zone.

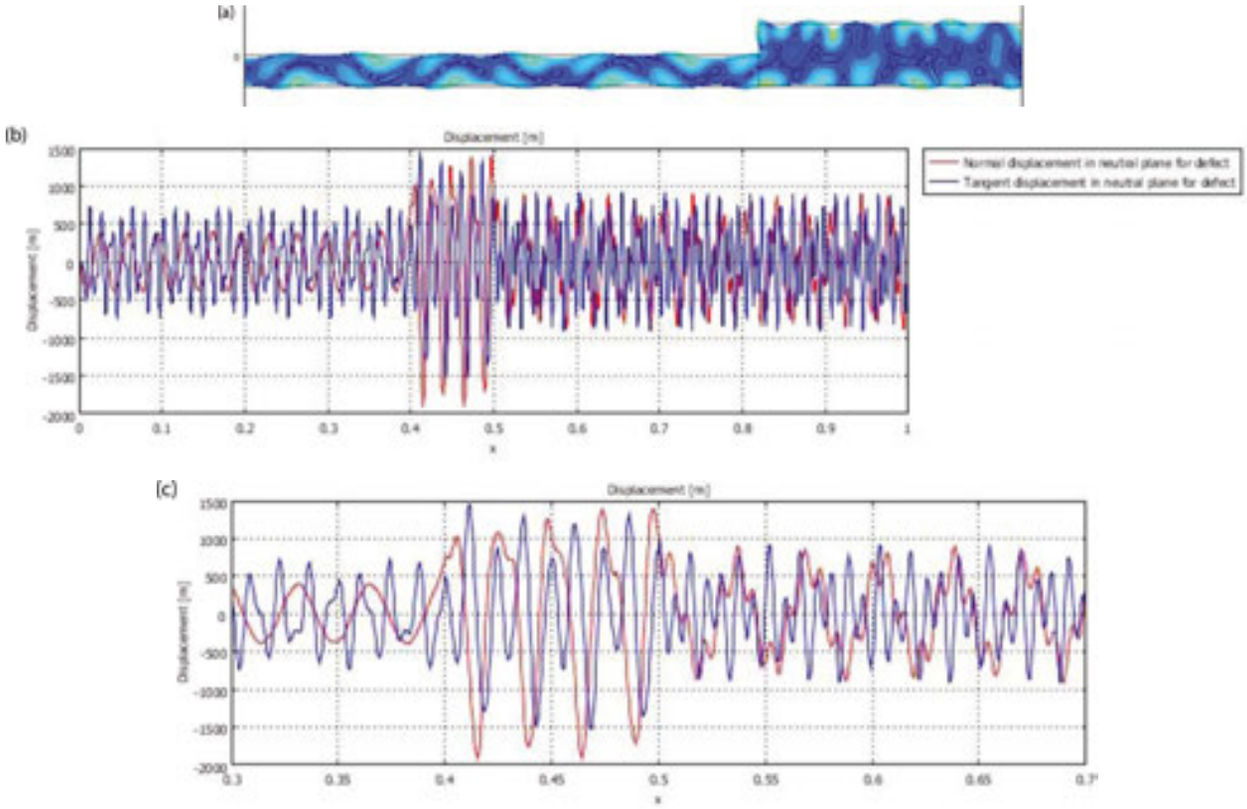

Figure 8. Displacement plots of the excited guided waves at 387.7 kHz. (a) Wave propagation-amplitude plot.(b) Displacement components at y=5 mm. (c) Zoom on the 5 mm thickness zone.

In the case of Lamb wave generation at the thickness reduction part of the plate, both S and A modes can propagate. Their detection is enabled by localising the region where the displacement shows a constant wave number.

The following conclusions may be drawn:

- At the excitation frequency of 214,9 kHz, the notch zone (5-mm thickness) shows a constant wave number. Both symmetric and asymmetric modes are observed in **Figure 9**.
- At the excitation frequency of 262,4 kHz, the main plate (10-mm thickness) shows a constant wave number. Both symmetric and asymmetric modes are observed.
- Both frequencies of 387,6 kHz and 360,9 kHz do not show any Lamb wave generation. Those resonances can be due to the natural frequencies of the plate.

This part of the work provided a good understanding of the behaviour of the defective plate when Lamb waves are generated. The following conclusions may be drawn:

- Although the excitation was designed to be mode-selective, both asymmetric and symmetric waves were excited.
- Each region of the plate with different thickness can excite Lamb wave separately from the rest of the structure.

http://dx.doi.org/10.5772/62985

3.3. Generation of the S0 and A0 modes in the transient regime

Results obtained in the transient regime must be validated. This excitation generates both symmetric and asymmetric modes. For different excitation frequencies using 10 cycle tune burst signal, the Fourier transform of the time response collected in the position at 0.5 m at the neutral plane of the plate was plotted (**Figure 9**).

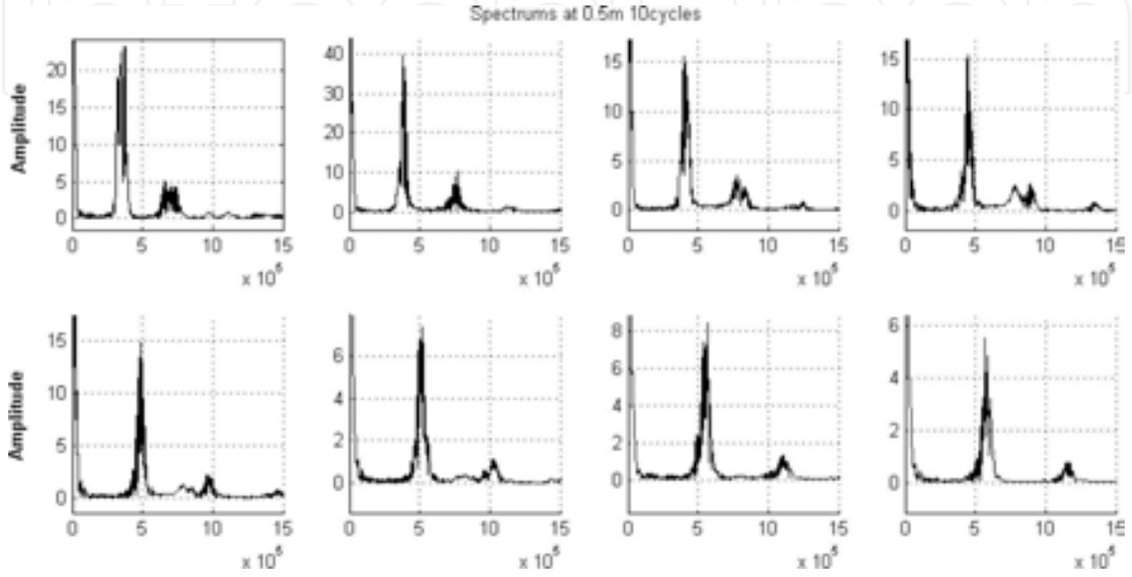

Figure 9. The different excitation frequency spectra.

Figure 9 clearly shows the existence of the two modes S0 and A0. The overlap of the different spectra is presented in **Figure 10** and shows that the maximum amplitude is obtained at a varying frequency, which depends on the excitation frequency.

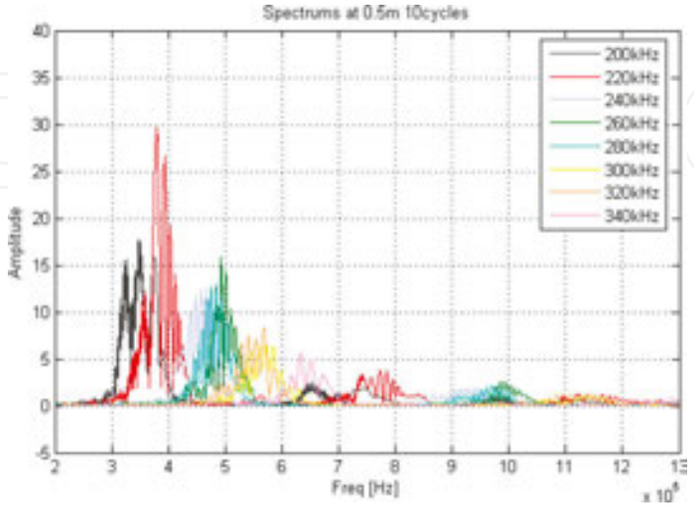

Figure 10. Superposition of the different excitation frequency spectra.

The results show the change in the frequency content introduced by the defect. Additionally, the work needs to be validated with experimental results. A 2D fast Fourier transform (2DFFT) is also used to identify the mode content of the different A-scans and compare them to 'Disperse' results.

3.4. Mode identification 2DFFT

The 2DFFT algorithm transforms a time/space representation into frequency/wave-number representation. It gives information about the mode content and the how dispersive the mode is.

Following on, a plate of 10-mm thickness is considered, excited using single point excitation. **Figure 11(a)** shows the results obtained using the 2DFFT, for the defect-free plate. S0, A0 and A1 modes are generated and this result is consistent with 'Disperse' results.

Figure 11(b) displays the dispersion curves for a plate that presents a thickness reduction of 5 mm, and shows the generation of additional modes S0 and A0.

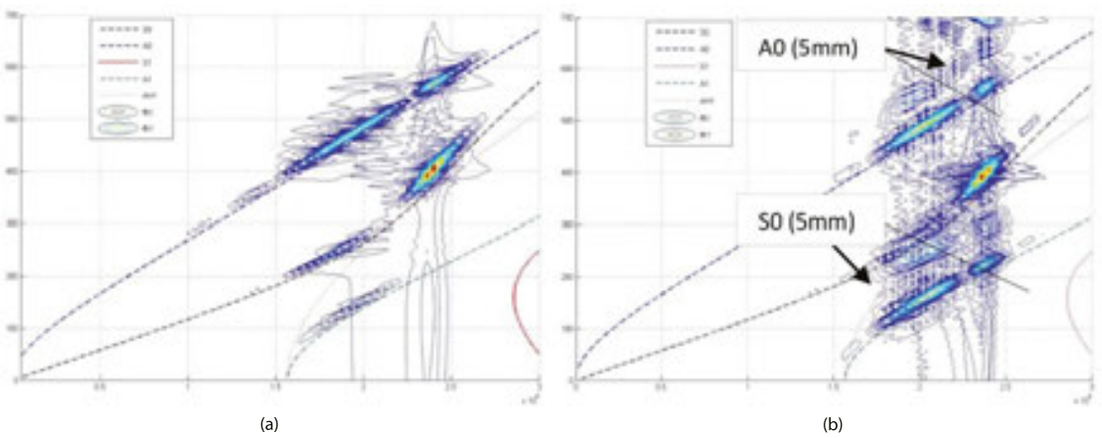

Figure 11. Validation of the 2dfft 2DFFT procedure for a plate of 10-mm thickness. (a) Compared to Disperse results. (b) 2DFFT for a 10-mm plate with 5-mm defect thickness over 20mm length.

The processing procedure is then clearly in good agreement with 'Disperse' and describes well with the problem under study. It was therefore used in the following development.

3.5. Transient modelling of the S0 mode propagation

Consider an excitation using seven-cycle tune-burst signal. Following 'Disperse', the dispersion curve for S0 gives a wavelength of 10 mm at 318,5 kHz and the dispersion curve for A0 gives a wavelength of 10 mm at 279,8 kHz.

The excited frequency bandwidth is about 100 kHz (**Figure 12**). It is noticed that A0, S0, A1 and S1 are generated and are in good agreement with 'Disperse'. AH1 and SH1 are not present in the results because the 2D model does not take the horizontal displacement components into account.

http://dx.doi.org/10.5772/62985

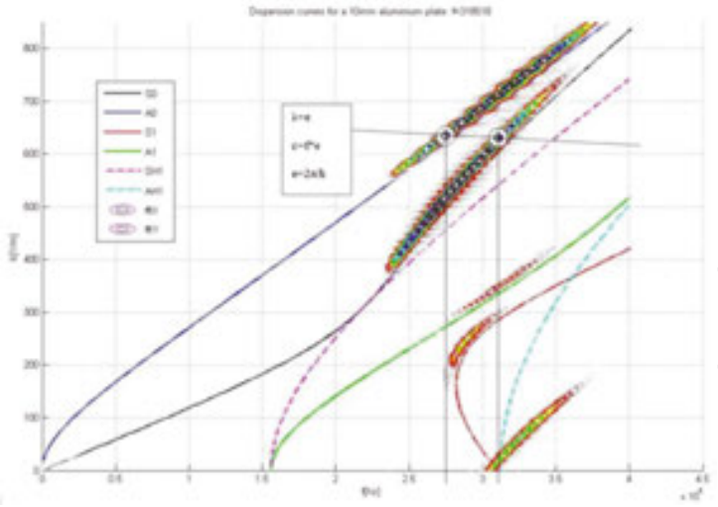

Figure 12. Dispersion curve generation using 2DFFT superimposed with Disperse results for a plate with constant thickness. The dashed lines are obtained from Disperse, and the surfaces plots are obtained from the 2DFFT.

Figures 13 and **14** give an extrusion plot at the frequency of 318,5 kHz and the A-scan at 0.2 m from the excitation location and the extrusion plot of the excited waves in the plate. Consider an excitation using seven-cycle tune-burst signal applied to the plate (10-mm thickness) with the 5-mm-thickness reduction. By applying the 2DFFT on the A-scan results at each position increment (**Figures 15** and **16**), the mode content of the GW generated in the plate is obtained. This is carried out for the frequencies of excitation of 279,8 and 318,5 kHz.

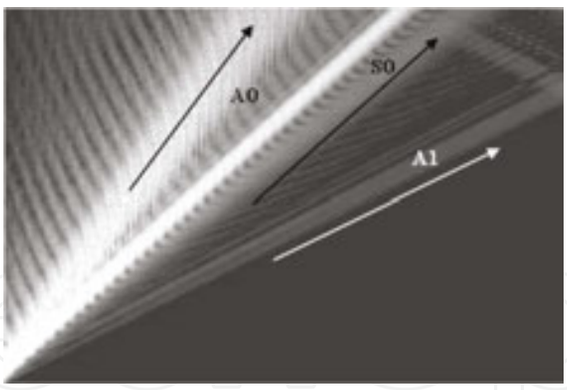

Figure 13. Extrusion of the wave propagation in the plate for the excitation frequency, f = 318,581kHz.

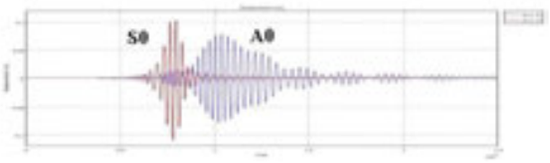

Figure 14. Displacement plot at 0.2 m from the excitation point.

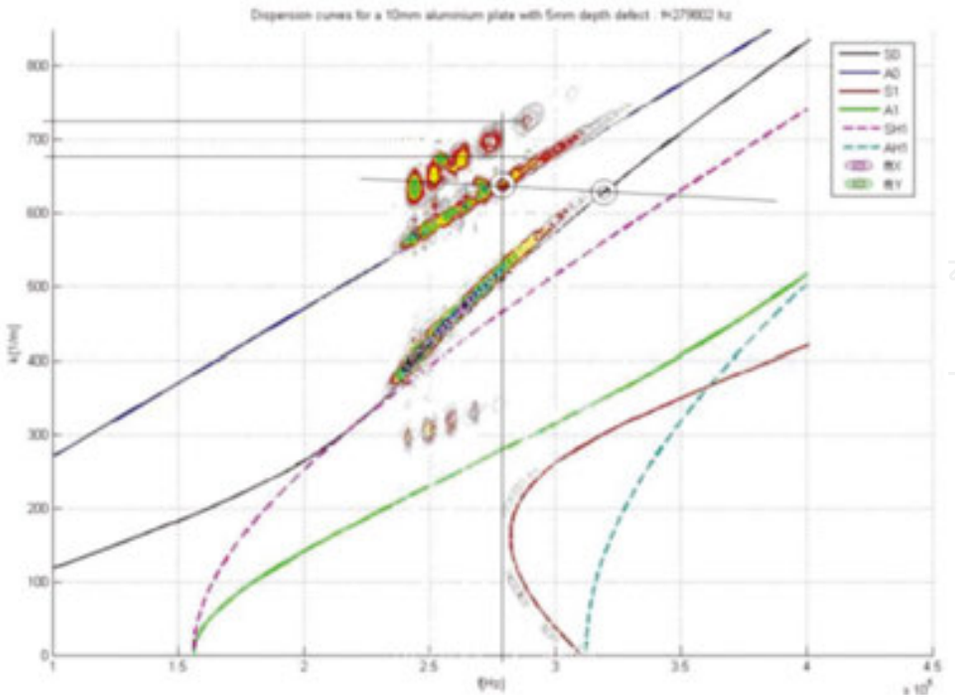

Figure 15. Dispersion curves generation for the defective plate at the excitation frequency 279.8 kHz using 10-cycle tune-burst signal. The dash lines are obtained from Disperse, and the surfaces plots are obtained from the 2DFFT.

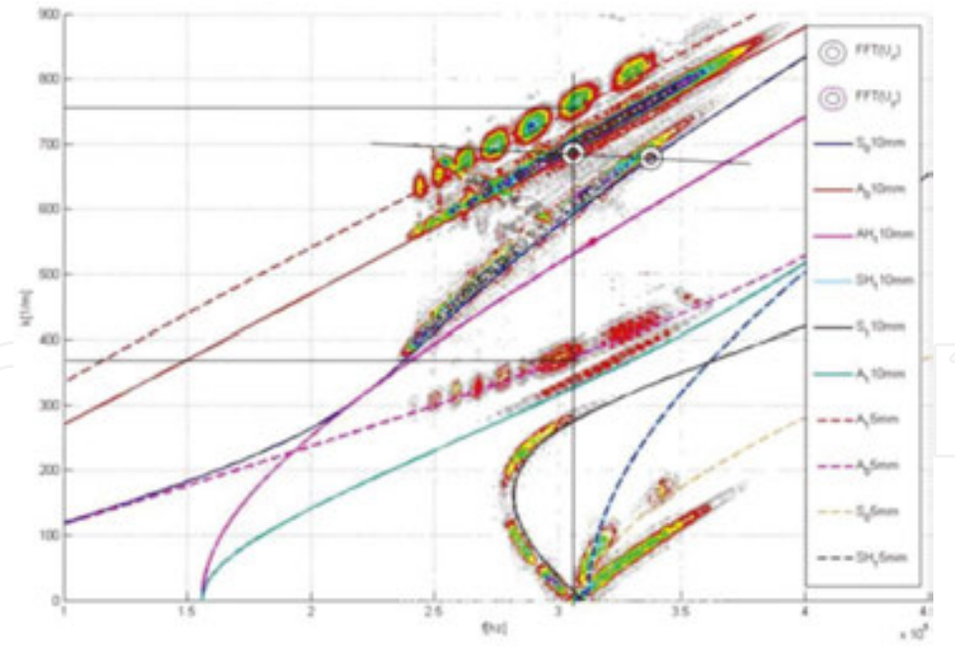

Figure 16. Dispersion curve generation for the defective plate at the excitation frequency of 318.5 kHz. using seven-cycle tune-burst signal. The dash lines are obtained from Disperse, and the surfaces plots are obtained from the 2DFFT.

The displacement extrusion and the A-scan at 0.2 m are presented in **Figures 17** and **18**. Additional modes near the dispersion curve A0 and S0 may be seen. These modes represent

http://dx.doi.org/10.5772/62985

the A0 and S0 modes of the part of the plate with 5-mm thickness. The results from 'Disperse' confirm this conclusion.

Figure 17 shows a complex wave generation and wave reflection. The main problem is that both symmetric and asymmetric waves are excited.

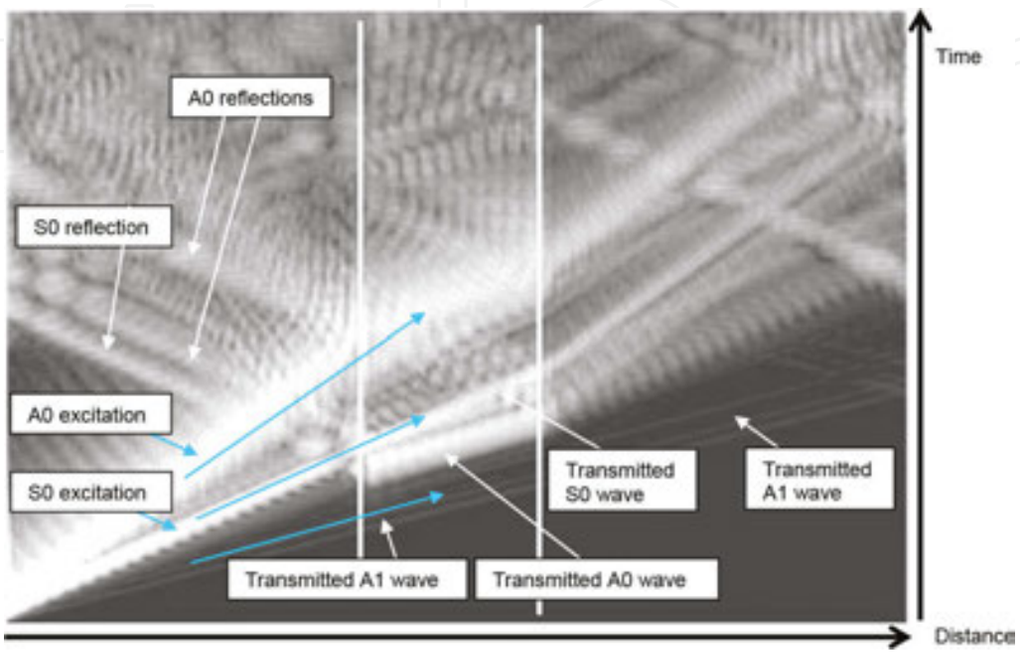

Figure 17. Extrusion of the displacement in the plate for the excitation, f = 318,5 kHz, 5-mm-notch thickness delimited by the white lines.

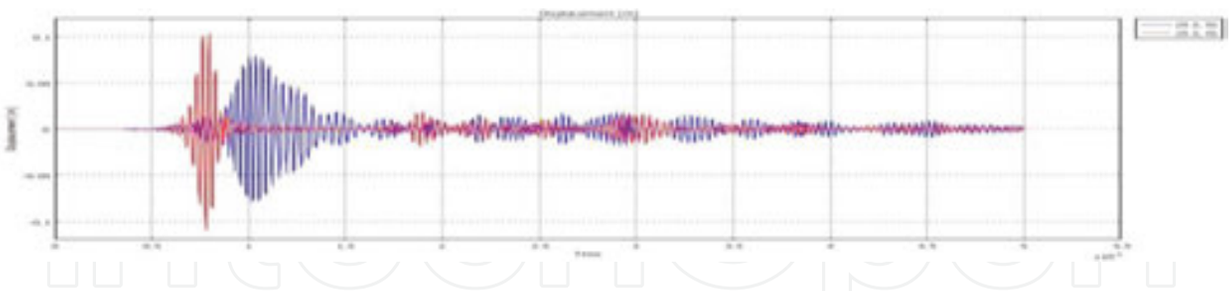

Figure 18. A-scan of the wave propagation in the plate for the excitation at the frequency, f=318.5kHz.

3.6. Mode selection

Using the procedure of mode selection described above, the same excitation was applied to A plate of10mm thickness with a 5mm thickness reduction.

The excited mode is now totally symmetrical, the dispersion curve plot in **Figure 21** is less complex and clearly shows the generation of additional modes due to the thickness reduction zone (**Figures 19** and **20**).

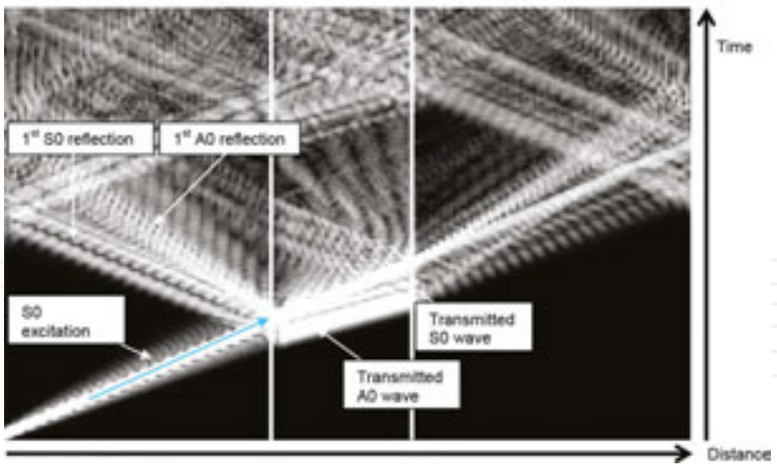

Figure 19. Extrusion of the displacement in the plate for the symmetric excitation at f = 318,5 kHz, 5-mm-notch thickness delimited by the white lines.

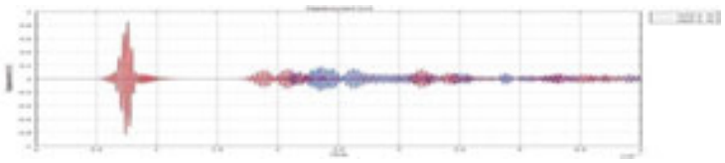

Figure 20. A-scan of the wave propagation in the plate for the symmetric excitation at the frequency, f = 318,581 Hz.

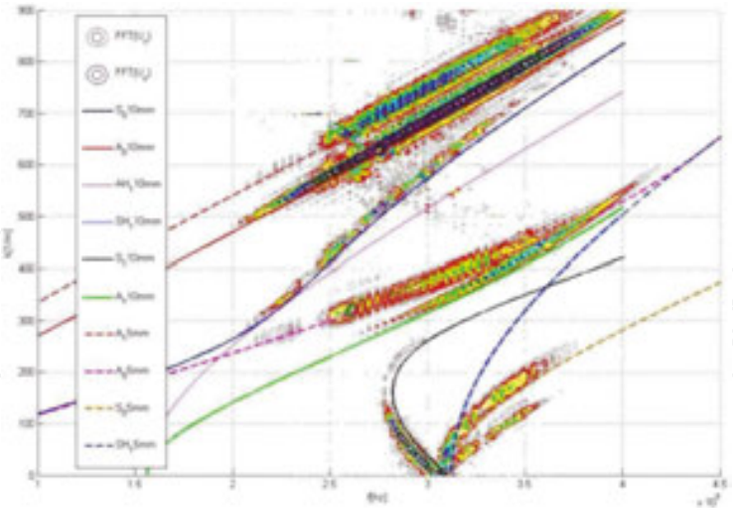

Figure 21. Dispersion curves generation using 2DFFT superimposed with Disperse results.

Figure 21 proves the generation of the additional S0 and A0 modes introduced by the thickness reduction zone. This conclusion is also demonstrated in the A-scan of **Figure 20**. As a result, the defect thickness is directly linked to the generated GW properties. This conclusion will be discussed in further detail in the last part of this work.

http://dx.doi.org/10.5772/62985

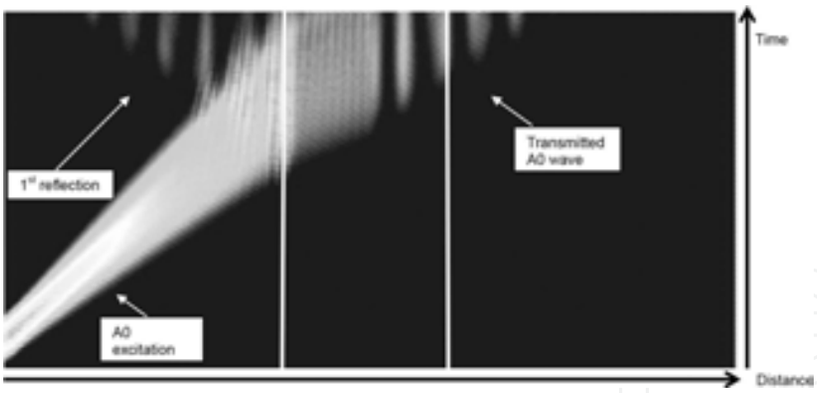

Figure 22. Extrusion of the displacement in the plate for the asymmetric excitation at f = 318,581 Hz, 5-mm-notch thickness delimited by the white lines.

Figure 22 presents the extrusion displacement plot of an asymmetric excitation of the plate with thickness reduction; it appears that this mode of excitation is too dispersive and cannot be used efficiently for inspection.

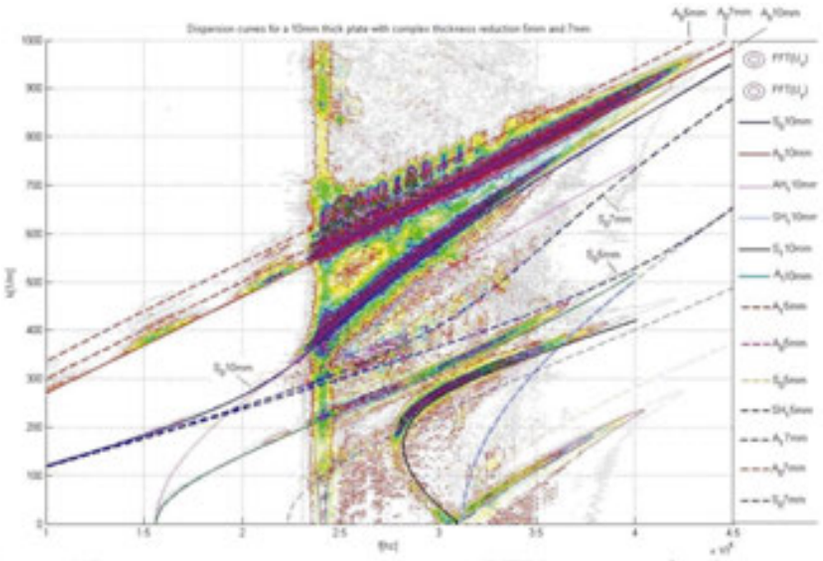

Figure 23. Dispersion curves generation using 2DFFT superposed to Disperse results. The dashed lines are obtained from Disperse, the surface plots are obtained from the 2DFFT.

Here a plate with reduction zones of different thicknesses was examined, which models a corroded area in an aluminium plate. The thickness levels considered here are 10, 7 and 5 mm in 15-cm-length regions as seen in **Figure 24**(top). For the point excitation mode, the extrusion of the displacement in **Figure 24** and the A-scan at 0.2m from the excited edge in **Figure 26**, are presented showing complex wave propagation and diffraction pattern. **Figure 25** presents the dispersion plots which seem to capture the change in thickness. The dispersion curves S0 and A0 are sensitive to the change of thickness from 10mm, 7mm to 5mm. It is clear that this feature relates to the thickness levels in the plate, and each thickness level introduces additional

modes with a phase velocity specific to the thickness reduction. From this phenomenon the NDT operator can get an idea of the corroded zone if the A-scan received contains additional echoes. In the practical work these additional echoes can be considered as noise or unknown indications, but following the present analysis it appears that they have significant meaning as indication of the presence of corroded areas or thickness modifications.

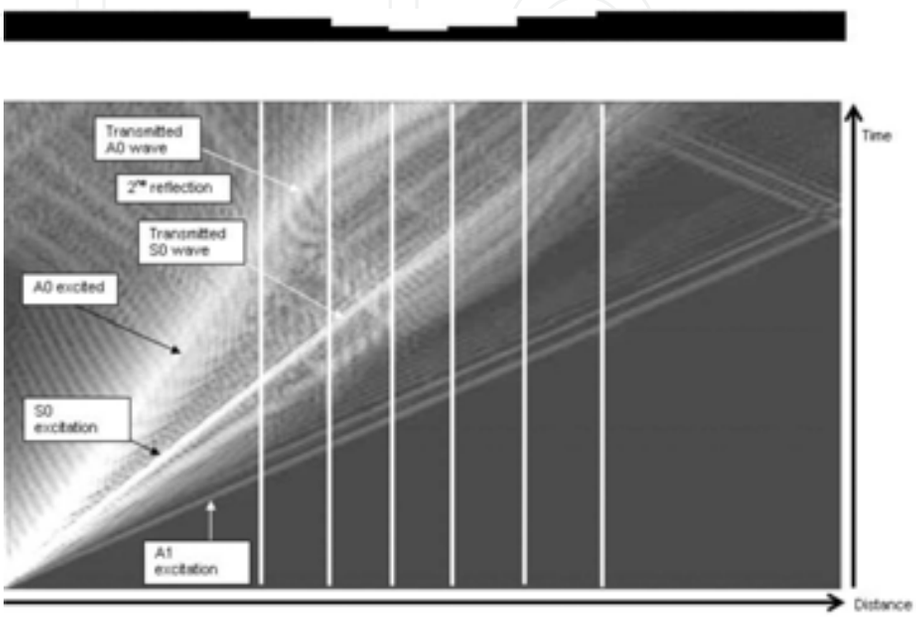

Figure 24. Extrusion of the displacement in the plate for the non-symmetric excitation at f = 318,5 kHz. 5, 7 and 10mm notch thickness delimited by the white lines.

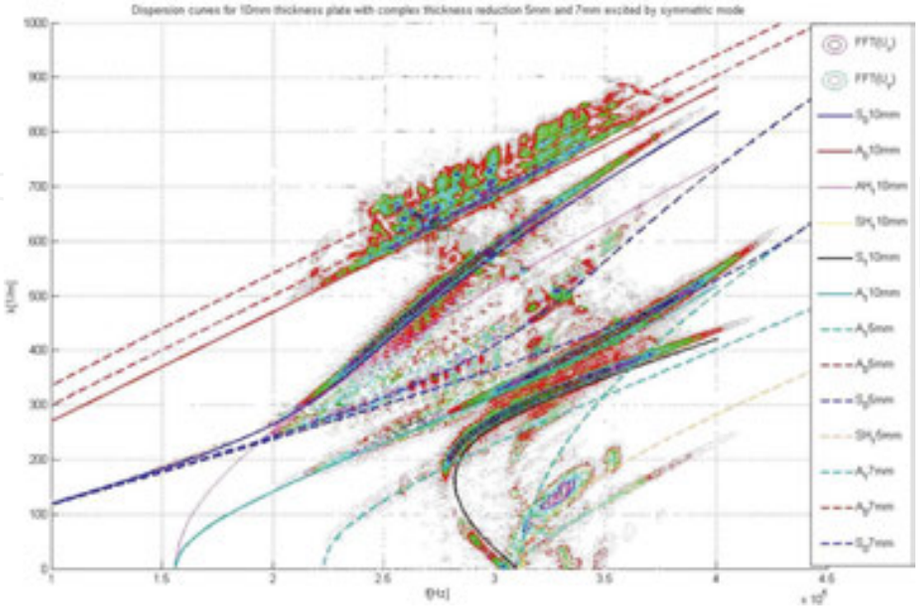

Figure 25. Dispersion curves generation using 2DFFT superimposed with Disperse results.

http://dx.doi.org/10.5772/62985

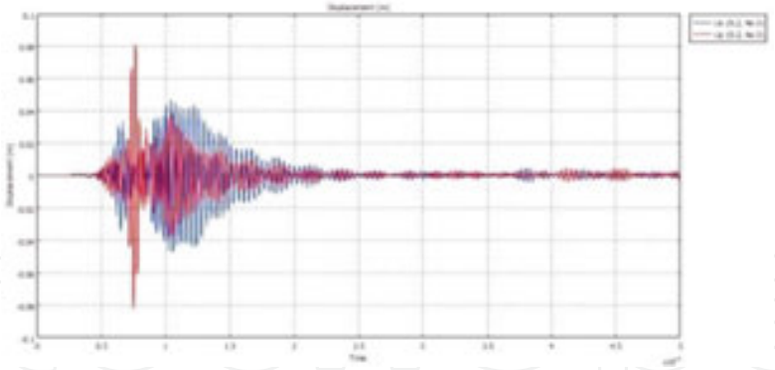

Figure 26. A-scan of the wave propagation in the plate with multi thickness defect for the non-symmetric excitation at the frequency f = 318,5 kHz.

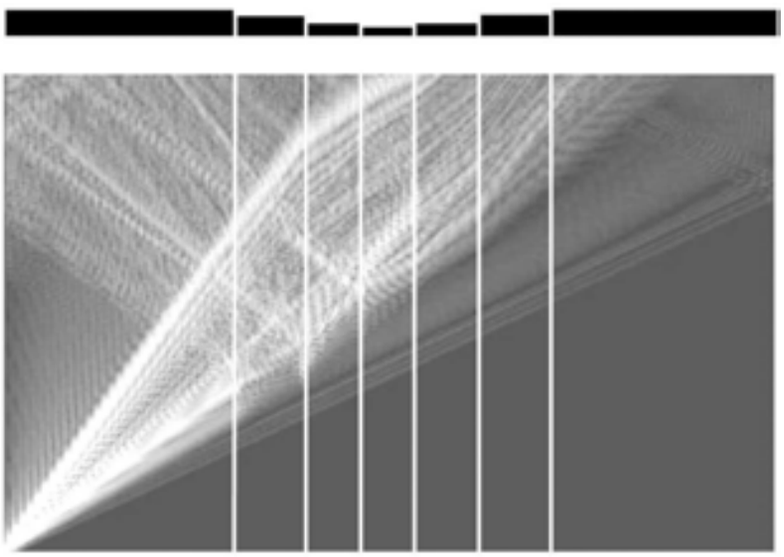

Figure 27. Extrusion of the displacement in the plate with complex thickness reduction zones.

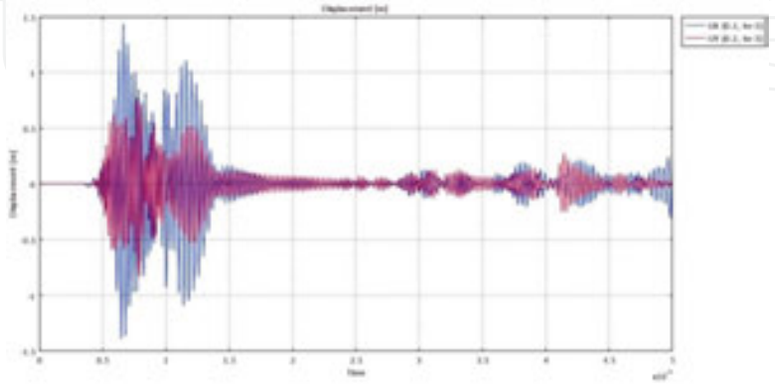

Figure 28. Dispersion curves generation using 2DFFT superimposed with Disperse results.

The final step in this work is to use symmetrical excitation instead of point excitation. The aim is to reduce the complexity of the excited mode which reduces the complexity of the A-scan analysis. The results are given in **Figures 27** and **28**. The echoes that indicate the presence of the corroded zone may be easily located in the A-scan of **Figure 28**.

4. Methodology

In this study the groundwork for the development of a fast, screening tool to detect corrosion defects by evaluating the effects of wall thinning has been presented. To analyse the response of LRU to corrosion, a two-dimensional finite element model was constructed including gradual thinning of the pipe walls. Experimental testing is necessary to validate the modelling results.

There is a wide range of applications where LRU can be applied to detect corrosion. Inspection tools can be used for in-service NDT and SHM. As mentioned at the beginning of this chapter, one of the most relevant uses of LRU is its application to pipeline integrity assessment. The experimental test to be described is based on this principle. Defect growth has been monitored by a novel system designed for this purpose. Specific tooling was designed in order to relate the effectiveness of the methodology (**Figure 29**). The system performs the total volume inspection more accurately than current methods of ultrasonic NDT inspection.

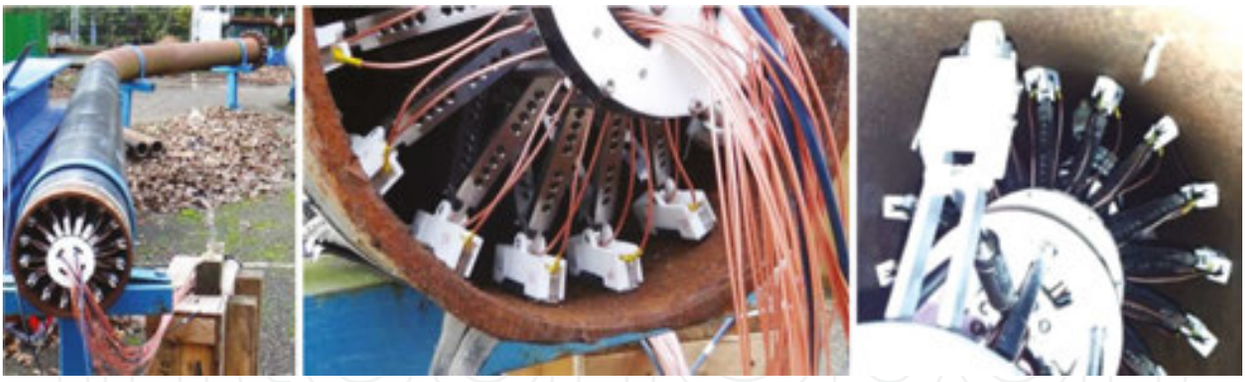

Figure 29. LRU collar for pipeline monitoring.

4.1. Experimental setup

Defects simulating wall thickness loss were introduced in the pipe at distances of approximately 1.2 and 2.4 m from the end of the transducers located at one end of the pipe segment. These defects simulated a through-thickness crack growth and an increased depth of a corroded area. The experimental results are presented in **Figure 30(a)**. The end-of-pipe amplitude reflection is reduced due to the increase of thickness loss at the location of the

http://dx.doi.org/10.5772/62985

simulated corrosion. In other regions of the A-Scans, there are several significant changes in the signal amplitude due to the loss of wall thickness. The most important aspect of the A-scan data is the amplified amplitude change due to a resonance that follows a trend with increasing deviation from the case with no damage. Investigating at the frequency domain of the signals with and without loss of wall thickness (**Figure 30(b)**), there is a greater loss of energy over a wider range of frequencies around 30 kHz compared to the results from the inserted cuts.

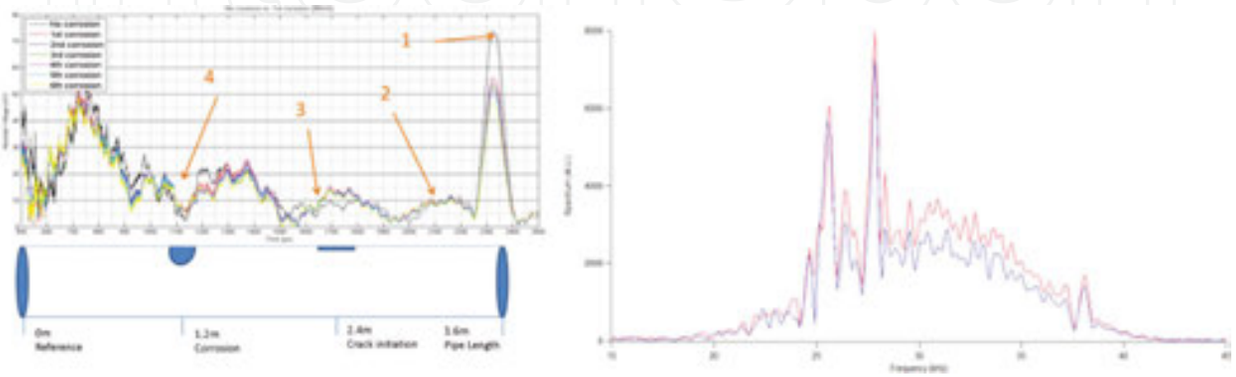

Figure 30. Simulated wall thickness loss in the outside surface of the 10″ pipe. The internal monitoring system being included inside the pipe for trials.

The additional presence of thickness loss on the outer wall of the pipe results in a loss of energy in the received end-of-pipe reflection. In the presence of wall thinning, there are significant changes in the amplitude of the A-scans at several points of the time-base. This is due to the creation of more complex wave behaviour within the pipe as the torsional wave interacts with the inserted feature.

4.2. Results

To validate the technique and the tooling, a crack was simulated with a slot increasing in depth in seven equal increments until the entire wall thickness was penetrated (**Figure 31**, measurements 1–7). A secondary defect simulating wall thickness loss was introduced on the outside wall of the pipe in six steps (**Figure 31**, measurements 8–13).

The results presented in an A-scan (**Figure 31(a)**) shown an end of-pipe reflection, which is reduced in amplitude in the presence of cracking and wall thinning, and as the width of the simulated corrosion is increased. In other regions of the filtered A-scan, where anomalies are present (**Figure 31(a)**), there are several significant increases in signal amplitude due to the loss of wall thickness. The A-scan amplitude changes, following an increasing trend deviation from the defect-free signal.

Investigating at the frequency domain of the signals with and without loss of wall thickness, there is a greater loss of energy over a wider range of frequencies around 30 kHz compared to the results from the inserted cuts and thinning.

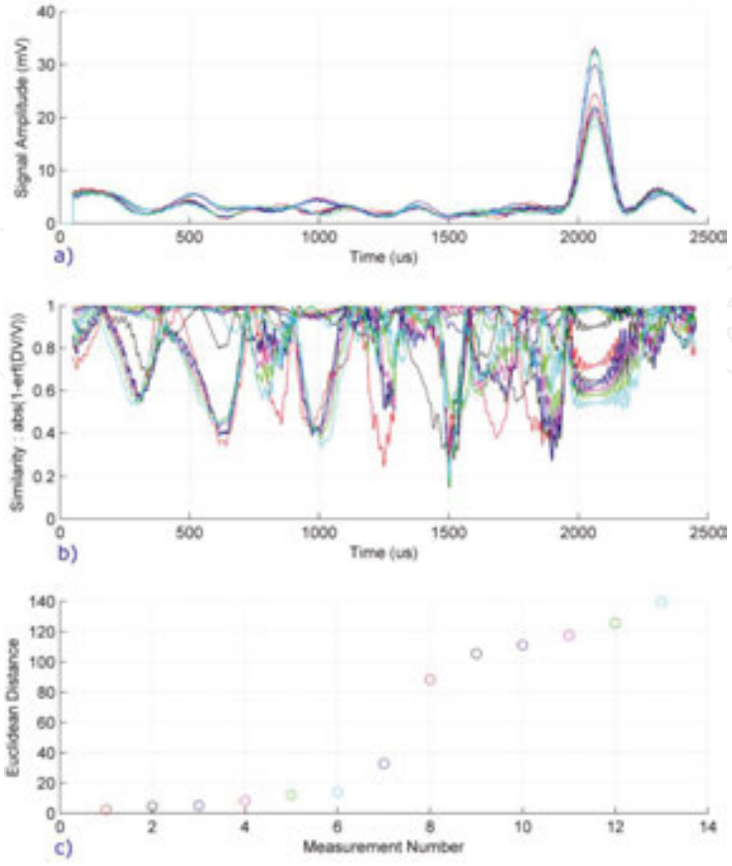

Figure 31. LRU monitoring results. Damage detection (a), similarity (b) and Euclidian distance (c).

Changes on the A-scan's amplitude reveal the presence of wall thickness loss. These different areas are evaluated by analysing the similarity of the signals at a given location.

Similarity is equal to one minus the error function of the rate of change of the A-scan's amplitude:

$$Similarity = 1 - erf\left(x\right) = \frac{2}{\sqrt{\pi}} \int_0^x e^{-t^2} dt, where x = \frac{V - V_0}{V_0}$$

Figure 31(b) shows the correlation between each of the signals acquired in comparison with the flawless pipe reference signal. The similarity is measured from one to zero, with one being equivalent to 100% equivalence of signals. The error is calculated in one dimension; thus, the similarity between two points on the real line is the absolute value of their numerical rate of change difference.

The Euclidean distances were analysed for one dimension, comparing the obtained signals on each measurement against the defect-free pipe signature. The distance between two points in one dimension is simply the absolute value of the difference between their coordinates. Mathematically, this is shown as follows:

http://dx.doi.org/10.5772/62985

$$Euclidean\ distance = \sqrt{|p1 - p2|^2}$$

where $p1$ is the first coordinate of the first signal and $p2$ is the first coordinate of the second signal.

In **Figure 31(c)**, the results show an increment in the distance between each signal measured and the reference signal when there is defect growth. The most important aspect considered is that the distance on amplitude change follows a trend with increasing deviation from the defect-free signal. GW allows rapid screening of long lengths of pipe to detect external or internal corrosion. Both large cracks and corrosion are detectable with GW technology. Depending on the position of the crack, the feature can go unnoticed when using only one GW mode. Corrosion can be detectable upwards from as little as 10% of cross section loss under certain conditions. The accuracy of detection is decreased by many factors such as distance, attenuation, scattering, absorption or leakage.

5. Conclusions

This chapter presents results on a 254-mm internal diameter pipe of 10-mm-wall thickness with a 82.9 cm2 Cross sectional Area (CSA). Artificial crack defects showed that significant increases in the signal-to-noise ratio of defect echoes can be obtained with this approach. Corrosion defects can be detected with thinning greater than 10% of wall thickness.

The alternative of using the resonance of LRU to obtain the thickness of each thinned area was investigated. The frequency at which each peak occurs is linked to the actual thickness producing the resonance. The method is to sweep the test frequency over a range which covers the nominal thickness and possible thinning ranges. The amplitude of the spectrum of the output across this range is defined and the existence of peaks determines the remaining wall thickness of the pipe. Different types of damage can be identified due to changes in received signal amplitude of the A-Scans compared to the time baseline.

This technique is then translated into a monitoring strategy that uses an internal monitoring robot (pig) in order to deploy ultrasonic sensors enabling the GW to propagate from inside the pipe and to reach unpiggable areas.

Author details

Ángela Angulo*, Slim Soua and Tat-Hean Gan

*Address all correspondence to: angela.angulo@twi.co.uk

TWI Ltd., Integrity Management Group, Condition and Structural Health Monitoring, Granta Park, Great Abington, Cambridge, UK

References

[1] Western European cross-country oil pipelines, Lyons D. 25yr performance statistics, CONCAWE oil pipelines management group. Report no. 1/02.

[2] Financial Times comment 'Growth in pipelines', May 2002

[3] Non-destructive Testing: An Expanding Market. 2002. Published by Business Communications Company. Web: www.buscom.com.

[4] European industry oil safety performance, statistical summary of reported incidents, Martin D E, Prepared for the CONCAWE, 1999. Safety Management Group

[5] Performance of cross-country oil pipelines in Western Europe, statistical summary of reported spillages, Davis P M. CONCAWE Oil pipelines Management Group, 1999. Special task force on pipeline spillages.

[6] European Commission, Directorate General, Institute for Health and Consumer Protection, 'Physical and Chemical Exposure Unit European Information System on Electromagnetic Fields Exposure and Health Impacts'. Final Report, February, 2005.

[7] Future growth prospects for inspection and repair, Fulop G. www.buscom.com.

[8] Lincoln Electric annual report 2001, www.lincolnelectric.com

[9] In-line inspection of hard-to-pig pipelines, Bukman F., Schmidt R. The Pipeline Pigging Conference, Amsterdam, The Netherlands, June 1997.

[10] PIGWaves – In–line service for internal inspection of unpiggable buried oil pipelines using long range ultrasound guided waves in fifty metre segments, TWI Case Study. www.twi-global.com.

[11] TWI Integrity Management Group, Collaborative Overview, July2014.

[12] Pipeline rupture and subsequent fire in Bellingham, Washington, Accident report NTSB/PAR-02/02, June1999.

[13] PR Newswire Aug 7th 2000. Following is a summary of press releases about Texas, Oklahoma, Louisiana and Arkansas companies and organizations transmitted today by PR Newswire.

[14] Review of Guided-wave Structural Health Monitoring. Ajay Raghavan and Carlos E. S. Cesnik The Shock and Vibration Digest 2007; 39; 91

[15] Strategies for Guided-Wave Structural Health Monitoring, A.J Croxford, P.D Wilcox, B.W Drinkwater, G Konstantinidis. 8 November 2007. DOI: 10.1098/rspa.2007.0048.

[16] A unified approach for the structural health monitoring of waveguides. Xuan Zhu, Piervincenzo Rizzo. Structural Health Monitoring November 2012 vol. 11 no. 6, 629-642.

[17] Ultrasonic Lamb wave tomography in structural health monitoring, Zhao X., Royer R., Owens S., Rose J. Smart Materials and Structures 2011, Volume 20, Issue 10, article id. 105002, 10 pp.

[18] Dispersion-based imaging for structural health monitoring using sparse and compact arrays, N Quaegebeur, P Masson, D Langlois-Demers and P Micheau. January 2011, Smart Materials and Structures, Volume 20, Number 2.

[19] Ultrasonics Classification of flaw severity using pattern recognition for guided wave based structural health monitoring, Corey A. Miller, Mark K. Hinders. Ultrasonics Volume 54, Issue 1, January 2014, Pages 247–258.

[20] Modelling of long range ultrasonic waves in complex structures. Slim Soua, Septimonette Chan, Tat-Hean Gan. TWI Ltd, Granta Park, Great Abington, Cambridge CB21 6AL, UK. BINDT annual conference 2008, 15-18 September 2008, Macclesfield, Cheshire, UK.

IntechOpen